Temporal variation and frequency dependence of seismic ambient noise on Mars from polarization analysis

Yudai Suemoto[1], Tatsunori Ikeda[1,2], Takeshi Tsuji[1,2,3] *

[1] Department of Earth Resources Engineering, Kyushu University, 744 Motooka, Nishi-ku, Fukuoka 819-0395, Japan

[2] International Institute for Carbon-Neutral Energy Research (WPI-I2CNER), Kyushu University, 744 Motooka, Nishi-ku, Fukuoka 819-0395, Japan

[3] Disaster Prevention Research Institute, Kyoto University, Gokasho, Uji, Kyoto 611-0011, Japan

Corresponding author: Takeshi Tsuji (tsuji@mine.kyushu-u.ac.jp)

Key points:

- A polarization analysis of InSight seismic data enables estimates of temporal variation and frequency dependence of ambient noise on Mars.
- Back-azimuths of low-frequency (<1 Hz) P-waves and Rayleigh waves show diurnal variations due to distant and nearby winds, respectively.
- The back-azimuth at high frequency points in the direction of the lander, indicating that wind-induced lander noise is dominant.

Abstract

We applied a polarization analysis of InSight seismic data to estimate the temporal variation and frequency dependence of the Martian ambient noise field. Low-frequency (<1 Hz) P-waves show a diurnal variation in their dominant back-azimuths that are apparently related to wind and the direction of sunlight in a distant area. Low-frequency Rayleigh waves (0.25–1 Hz) show diurnal variations and a dominant back-azimuth related to the wind direction in a nearby area. Low-frequency signals that are derived mainly from wind may be sensitive to subsurface structure deeper than the lithological boundary derived from an autocorrelation analysis. On the other hand, dominant back-azimuths of high-frequency (>1 Hz) waves point toward the InSight lander, especially in daytime, indicating that wind-induced lander noise is dominant at high frequencies. These results point to the presence of several ambient noise sources as well as geologic structure at the landing site.

Plain Language Summary

Seismic ambient noise (microtremors) is continuously generated not only on Earth but also on Mars. We used data from the seismometer on the InSight lander to make estimates of microtremor characteristics and identified possible underground structures that influence the propagation of microtremors. Low-frequency P-waves derived from microtremors show daily variations that appear to be induced by wind and changes of sunlight during the Martian day in distant areas, whereas low-frequency Rayleigh waves show daily variations that may be generated by wind in nearby areas. High-frequency signals appear to originate from vibrations of the lander associated with wind. Microtremors in other frequency ranges have different characteristics. These results suggest that depending on their frequency, microtremors can be induced by wind and other sources, and may then be influenced by geological structures. This study demonstrates that ambient noise data will be helpful for imaging and monitoring Mars' interior structure and natural resources, such as ice deposits, without the need for data from marsquakes and artificial seismic sources.

Keywords: InSight, ambient noise, polarization analysis, autocorrelation function, wind

1. Introduction

When NASA's Interior Exploration using Seismic Investigations, Geodesy and Heat Transport (InSight) lander touched down in Elysium Planitia on 26 November 2018, it went on to deploy a geophysical observatory on Mars. One of its primary scientific investigations is the Seismic Experiment for Interior Structure (SEIS; InSight Mars SEIS Data Service, 2019; Lognonné et al., 2019). The lander also includes a set of environmental sensors, including temperature and wind sensors (Banfield et al., 2019; Spiga et al., 2018). The InSight seismometer has detected several hundred marsquakes, most of them much smaller than earthquakes typically felt on Earth, but some were nearly as large as magnitude 4 (Witze, 2019). The instrument is especially useful to identify small earthquakes at night, when the strong ambient noise generated during the day by wind is subdued (Witze, 2019). Martian ambient noise detected by the seismometer on the Viking 2 lander has been correlated with wind speed (Anderson et al. 1977; Nakamura and Anderson, 1979). However, that seismometer did not obtain seismic signals directly because it was deployed on the lander and not on the surface (Knapmeyer-Endrun et al., 2017).

Analysis of seismic ambient noise is a technique widely used on Earth to image and monitor the subsurface (e.g., Nimiya et al., 2017; Nishida et al., 2008), and several studies have made similar use of ambient noise on the Moon (e.g., Larose et al., 2005; Tanimoto et al., 2008). If ambient noise can be used to image and monitor the interior structures of Mars, this technique will be a powerful tool because it does not require any natural marsquakes or expensive artificial seismic sources.

In this paper, we characterize the ambient noise on Mars relying on the recent data from the InSight seismometer. We applied a polarization analysis to the InSight seismic records (InSight Mars SEIS Data Service, 2019) to extract the dominant back-azimuth and directional intensity of ambient noise (Takagi et al., 2018). Furthermore, by comparing the characteristics of Rayleigh waves with autocorrelation functions (i.e., reflectivity), we achieved insight into the relationship between lithology and the sensitive frequency of Rayleigh waves included in ambient noise. By demonstrating the feasibility of ambient noise methods on Mars, this study shows that future seismic network projects on Mars will contribute to not only modeling and monitoring of Mars' interior structure, but also exploration for Martian resources (e.g., ice deposits).

2. Data and Method

2.1. Data Preparation

The SEIS instrument includes a long-period, very broad band seismometer (SEIS-VBB) with a sampling rate of 20 Hz and a natural frequency of 0.5 Hz (Lognonné et al., 2019; InSight Mars SEIS Data Service, 2019). This seismometer was placed in Elysium Planitia in particular to satisfy the constraints on landing safety and the instrument deployment requirements (Golombek et al., 2017). In this study, we used continuous seismic records from SEIS-VBB between February and June 2019. We corrected the data for the instrumental response using ObsPy (Beyreuther et al., 2010). The SEIS-VBB is a triaxial seismometer in which the three mutually perpendicular pendulums are mounted obliquely. Therefore, our first step was to numerically rotate the axes of the seismometer and construct seismic records with vertical and horizontal components (see Text S1 in the supporting information).

We then converted the seismic data from Earth time (UTC; Coordinated Universal Time) to the Mars time domain (LMST: Local Mean Solar Time) by using the procedures of Allison (1997) and Allison and McEwen (2000). The power spectral density on Mars calculated from ambient noise shows that the noise on Mars is lower at most frequencies than that of the Earth noise model (see Fig. S1 in the supporting information). The power spectral densities of the horizontal and vertical components from Sols 194 to 197 (**Fig. 1**) are an example of the typical daily cycle, in which signal amplitudes are greater during the day than during the night. On Mars, high variability of wind in daytime is caused by convective mixing in the planetary boundary layer that results from near-surface gradients of atmospheric temperature (e.g., Smith et al., 2006; Spiga et al., 2018). At frequencies higher than ~1 Hz, we observed large noise amplitudes in narrow frequency ranges. These local noise peaks correspond to the elastic resonances of the lander excited by the wind (Murdoch et al., 2017; Lognonné et al., 2020). These results demonstrate that the amplitude of ambient noise is strongly associated with the wind strength.

We divided continuous seismic data into 1-min segments because short time windows are suitable to remove glitches and other high-amplitude signals (Takagi et al., 2018). We excluded time segments whose root-mean-squared (RMS) amplitudes exceeded 10 times the median RMS amplitude, treating daytime hours (from 6:00 to 18:00 LMST) and nighttime hours (from 18:00 to 6:00 LMST) separately because the surface wind velocity was high during the daytime at the InSight landing site (**Fig. 1**) as anticipated by Spiga et al. (2018).

2.2. Polarization Analysis

We conducted a polarization analysis of the ambient seismic wave field recorded by the InSight station using the method developed by Takagi et al. (2018). This analysis uses a simple relationship between the vertical-horizontal cross spectra and the azimuthal energy distributions of incident waves in ambient noise. The real part of the cross spectra is related to linearly polarized waves and the imaginary part is related to elliptically polarized waves. We computed vertical-horizontal cross spectra from 1-min segments data using the equations

$$\Phi_{ZN} = \frac{u_Z^* u_N}{u_Z^* u_Z}, \tag{1}$$

$$\Phi_{ZE} = \frac{u_Z^* u_E}{u_Z^* u_Z}, \tag{2}$$

where Φ is the vertical-horizontal cross spectrum, u is the seismic record in the frequency domain of each component, and the subscripts Z, N and E indicate vertical, north-south and east-west component, respectively. The asterisk indicates the complex conjugate. The cross spectra are normalized by the power spectra of the vertical component so as to equally weight each data segment. In this study, the cross spectra were calculated at each frequency and the results were averaged within each of six single-octave frequency bands: 0.125–0.25, 0.25–0.5, 0.5–1, 1–2, 2–4 and 4–8 Hz.

Following Takagi et al. (2018), the dominant direction and directional intensity of a Rayleigh wave (elliptically polarized wave) are given by

$$\varphi_{R1} = arctan\left(\frac{Im\langle\Phi_{ZE}\rangle}{Im\langle\Phi_{ZN}\rangle}\right) + \pi, \tag{3}$$

$$A_{R1} = \sqrt{(Im\langle\Phi_{ZN}\rangle)^2 + (Im\langle\Phi_{ZE}\rangle)^2}, \tag{4}$$

and for a P-wave (linearly polarized wave) by

$$\varphi_{P1} = arctan\left(\frac{Re\langle\Phi_{ZE}\rangle}{Re\langle\Phi_{ZN}\rangle}\right) + \pi, \tag{5}$$

$$A_{P1} = \sqrt{(Re\langle\Phi_{ZN}\rangle)^2 + (Re\langle\Phi_{ZE}\rangle)^2}, \tag{6}$$

where $\langle\rangle$ denotes the ensemble average and φ_{R1} and φ_{P1} represent the phase angles of first-order terms of the azimuthal power spectra added to π, which provide the dominant back-azimuths of Rayleigh waves and P-waves, respectively. A_{R1} and A_{P1} indicate the amplitudes of the first-order terms representing the intensity of the directionality of the Rayleigh wave and P-wave, respectively.

In the determination of Rayleigh wave azimuth, there is a 180-degree ambiguity depending on the direction of motions (prograde or retrograde). To evaluate the motion of Rayleigh waves on Mars, we computed analytical solutions of Rayleigh waves for the layered model of Knapmeyer-Endrun et al. (2017) of the InSight landing site (see Text S2 and Fig. S2 in the supporting information). The results indicate that the fundamental mode of Rayleigh waves with retrograde motions is mostly dominant in our analyzed frequency range, whereas the first higher mode with prograde motions is dominant at some frequencies higher than 4 Hz. We therefore defined the azimuth of Rayleigh waves assuming retrograde motions, although the first higher mode with prograde motions might influence our results at frequencies higher than 4 Hz. Note that the azimuth of prograde or retrograde Rayleigh waves depends on the sign of the exponent in the Fourier transform. We used equation (3) to estimate the back-azimuth of retrograde Rayleigh waves because our analysis used the Fourier transform with a negative exponent. Shear waves with displacement in the vertical-horizontal plane (SV-waves) also contribute to vertical-horizontal cross-spectra (Takagi et al., 2018). Vertically incident SV-waves contribute to the real part of the vertical-horizontal cross spectra, whereas horizontally incident SV-waves with post-critical incident angles contribute to the imaginary part. For simplicity, we assumed that the contribution of P-waves is dominant in the real part of the cross spectra and the contribution of Rayleigh waves is dominant in the imaginary part. Under the assumption that Rayleigh and Love waves are random uncorrelated waves, Love waves make no contribution to vertical and horizontal cross spectra (Takagi et al., 2018).

2.3. Autocorrelation Analysis

To estimate the geological structure beneath the InSight landing site, we applied autocorrelation analysis to the vertical and horizontal motions of the seismometer record. Autocorrelation of ambient noise records yields the zero-offset shot gather (e.g., Minato et al., 2012; Wapenaar & Fokkema, 2006). The method assumes that the noise source is randomly distributed and mutually uncorrelated for different source positions (e.g., Roux et al., 2005; Wapenaar and Fokkema, 2006; Weaver & Lobkis, 2004). In this analysis, we applied a bandpass filter of 5–7 Hz to each component record of 1-min segments, because we found clear reflectors of autocorrelation function in that frequency band. Furthermore, we sought to find and integrate information independent of the polarization analysis for the investigation of the lander site. We applied one-bit normalization (e.g., Bensen et al., 2007) to ensure the exclusion of energetic signals. We calculated autocorrelation functions of the vertical component and the horizontal components in each sol to extract P- and S-wave reflections, respectively. Even if the lander near the seismometer generates vibration and becomes a noise source, the autocorrelation analysis with one-bit normalization reduces the influence of the source but enhances the contribution of reflected waves from the source. Thus, we expect that autocorrelation analysis is suitable for subsurface imaging.

3. Results

Figures 2a and 2b show the temporal variations of dominant back-azimuths and directional intensity of P-waves and Rayleigh waves from Sols 75 to 211 in the six frequency bands. The cross spectra are averaged for each hour in the Mars time domain (LMST). The dominant back-azimuths were different for each frequency band. The directional intensity of Rayleigh waves was less than that of P-waves in all frequency bands.

To illustrate the daily temporal variation, we present results from Sols 194 to 197 (**Fig. 3**). For low-frequency P-waves (<1 Hz), the back-azimuths shifted between east and north during the course of the day (**Fig. 3a**). The back-azimuths at the lowest frequencies pointed southeast in daytime, roughly consistent with the wind direction. At night, the back-azimuths of 0.25–1 Hz P-waves usually pointed east, except just after sunset; more precisely, they differed notably from the wind direction at night, pointing east several hours before sunrise and pointing west to north after sunset. For 0.25–1 Hz Rayleigh waves (**Fig. 3b**), the back-azimuth pointed southwest before sunrise, south or southeast during the day, and southwest at night, similar to the wind direction.

At high frequencies (>1 Hz), the dominant back-azimuths of P-waves (**Fig. 3a**) pointed northeast in daytime, as did the back-azimuths of high frequency Rayleigh waves (>2 Hz). As we discuss later, the Insight lander is located northeast of the seismometer.

Figure 4 shows the temporal variation of the autocorrelation function during the observation period. The autocorrelation function of the vertical component (**Fig. 4a**) indicates the presence of reflectors at 0.6 s and 1.1 s. Because these reflectors persisted throughout the observation period, they appear to be reliable and may represent a lithological boundary that imposes a contrast in acoustic impedance. The autocorrelation functions of the two horizontal components (**Figs. 4b and 4c**) display dominant reflectors at 1.1 s. They show evidence of polarization anisotropy of S-waves, in that the reflector at ~1.1 s is more prominent in the EW component (**Fig. 4c**) than in the NS component (**Fig. 4b**).

4. Discussion

The temporal variation of the dominant back-azimuth of <1 Hz P-waves could be related to the direction of sunlight (or related thermal effects) in addition to the wind direction when noise derived from the lander is absent. During the several hours before sunrise, the area east of the lander site is in daylight and the wind speed is high, thus the dominant P-wave back-azimuth could point east before sunrise (**Fig. 3a**). This interpretation would also explain the westward P-wave back-azimuth after sunset, although the back-azimuths are scattered from west to north. These results demonstrate that low-frequency P-waves observed at the InSight site may be derived from wind and insolation effects (e.g., thermal cracking) in distant areas. Indeed, P-waves on Earth are strongly influenced by distant events (Takagi et al., 2018). Seismic sources induced by temperature variation are capable of generating low-frequency ambient noise.

Because the variation of the directionality of 0.25–1 Hz Rayleigh waves was closely related to the wind direction (**Fig. 3b**), low-frequency Rayleigh waves were likely derived from winds relatively close to the seismometer. The back-azimuth of Rayleigh waves could be influenced by the radiation pattern of Rayleigh waves. Assuming that horizontal single forces exerted in the wind directions on rough surface topography excited seismic waves including Rayleigh waves, a symmetric radiation pattern (i.e., with 180-degree ambiguity) could be expected in the back-azimuths (**Fig. 3b**). Although stacking the cross spectra for each hour improves the stability of estimated dominant back-azimuths (**Fig. 3b**), using shorter time windows could make it possible to extract secondary dominant back azimuths. To investigate this possibility, we computed the back-azimuth from every 1-min segment (**Fig. S3** in supporting information). The results of this exercise show that directionalities of 0.125–1 Hz Rayleigh waves have two trends 180 degrees apart during certain periods; thus, the radiation pattern of Rayleigh waves could influence the observed back-azimuth. Rayleigh waves in the 0.25–1 Hz range would be sensitive to the depth range of 0.8–3.2 km, if we assume a Rayleigh wave velocity of 2400 m/s (Knapmeyer-Endrun et al., 2017). Therefore, the wind may be responsible for 0.25–1 Hz Rayleigh waves that are sensitive to the crustal structure beneath the shallow regolith layer.

At high frequencies, the back-azimuths of P-waves >1 Hz and Rayleigh waves >2 Hz are northeast in daytime. The direction is consistent with the location of the InSight lander (**Fig. 3**), which generates mechanical noise as wind acts on the lander (Murdoch et al., 2017; Lognonné et al., 2020). If wind-induced lander noise is dominant at high frequencies, it would be difficult to observe high-frequency Rayleigh waves with the seismometer because the distance between the lander and the seismometer is too short (several meters) for surface waves to emerge. Therefore, instead of referring to “P- and Rayleigh waves” in high-frequency (>1 Hz) results, it is preferable to refer to “linearly and elliptically polarized components of observed waves” as we have in **Figs. 2 and 3**.

These frequency-dependent variations of ambient noise characteristics could be mainly related to ambient noise sources and lithology beneath the seismometer. Ambient noise on Earth is caused by wind (Lepore et al., 2016) as well as ocean gravity waves, volcanic activity, and anthropogenic sources (e.g., Longuet-Higgins, 1950; Takagi et al., 2018; Nimiya et al., 2017; Nakata et al., 2019). Before the InSight project, a main source of ambient noise on Mars was expected to be the direct interaction between the atmosphere and the solid surface of the planet (Knapmeyer-Endrun et al., 2017). On the Moon, high-frequency Rayleigh waves are induced by ambient noise resulting from thermal events (Larose et al., 2005; Tanimoto et al., 2008). On Mars, there are numerous small craters near the InSight landing site (Warner et al., 2016) that could be locations of thermally triggered soil slumping (Knapmeyer-Endrun et al., 2017) that could generate high-frequency surface waves. Thus wind-induced noises, thermal effects, surface pressure, or other sources may induce the ambient noise around the InSight landing area.

To further consider the relationship between the frequency dependence of Rayleigh waves (**Fig. 3b**) and the lithology of the site, we investigated the autocorrelation results (**Fig. 4**), in which several reflectors beneath the InSight landing site are evident. The P-wave reflectors at 0.6 and 1.1 s in the vertical component (**Fig. 4a**) are stable, suggesting the existence of a significant lithological boundary. Furthermore, an S-wave reflector appeared at 1.1 s in the horizontal component results (**Fig. 4b and 4c**). If the 1.1 s S-wave reflector is the same as the 0.6 s P-wave reflector, we can estimate the ratio of ~1.83 between the P-wave and S-wave velocities. Because we cannot estimate the seismic velocity of the subsurface formation, we cannot accurately estimate the depth of the reflectors from the autocorrelation functions. However, we can estimate the frequency of Rayleigh waves that are sensitive to the depth of a reflector from the autocorrelation function. Under the assumption that the autocorrelation function of the horizontal component represents S-wave reflectivity, the depth of a reflector at two-way travel time t can be estimated as $Z = t\ V_S/2$, where V_S is S-wave velocity. The sensitive depth of Rayleigh waves is $Z = 1/3\ \lambda$ (or $Z = V_S/3f$) (e.g., Foti et al., 2014; Hayashi, 2008), where λ is wavelength and f is frequency. Therefore, the sensitive frequency of a Rayleigh wave for a reflector at two-way travel time t can be estimated as $f = 2/(3t)$. From this relationship, the frequency of a Rayleigh wave that is sensitive to a 1.1 s reflector shown in **Figs. 4b and 4c** can be estimated as ~0.6 Hz. Below 0.6 Hz, the azimuths of Rayleigh waves are associated with wind direction. Therefore, Rayleigh waves that are sensitive to depths beneath the lithological boundary identified by reflectivity could be extracted from wind-induced ambient noise. However, it would be difficult to extract Rayleigh waves propagating above the lithological boundary close to the landing site, because they are contaminated by lander-induced noise.

5. Conclusions

We have conducted a polarization analysis of InSight seismic data to estimate temporal variations of the ambient noise field on Mars. Our findings are these:

- Low-frequency (<1 Hz) P-waves show a diurnal variation, and the dominant back-azimuth is related to the wind and the direction of sunlight in distant regions.
- Low-frequency (0.25–1 Hz) Rayleigh waves show a diurnal variation, and the dominant back-azimuth points toward the wind direction in nearby regions.
- The dominant back-azimuth at high-frequency (>1 Hz for linearly polarized components and >2 Hz for elliptically polarized components) points in the direction of the lander, indicating that the wind-induced lander noise is dominant.

These results suggest that the dominant sources of ambient noise on Mars differ with frequency and wave type, and there may be several different ambient noise sources despite the absence of oceans on Mars. The high repeatability of P-waves and Rayleigh waves derived from ambient noise suggests the feasibility of utilizing ambient noise for subsurface imaging and monitoring on Mars. Further studies are necessary to clarify the contribution of SV-waves in ambient noise on Mars, which influences the results of our polarization analysis.

Acknowledgement

We acknowledge NASA, CNES, their partner agencies and Institutions (UKSA, SSO, DLR, JPL, IPGP-CNRS, ETHZ, IC, MPS-MPG) and the flight operations team at JPL, SISMOC, MSDS, IRIS-DMC and PDS for providing SEED SEIS data. We used the seismometer data from IRIS-DMC. The wind and temperature data were downloaded

from the following URL; https://atmos.nmsu.edu/data_and_services/atmospheres_data/INSIGHT/insight.html#Selecting_Data.

This study was supported through JSPS KAKENHI grant 20H01997.

References

Allison, M. (1997). Accurate analytic representations of solar time and seasons on Mars with applications to the Pathfinder/Surveyor missions. *Geophysical Research Letters*. https://doi.org/10.1029/97GL01950

Allison, M., & McEwen, M. (2000). A post-Pathfinder evaluation of areocentric solar coordinates with improved timing recipes for Mars seasonal/diurnal climate studies. *Planetary and Space Science*, *48*(2–3), 215–235. https://doi.org/10.1016/s0032-0633(99)00092-6

Anderson, D. L., Miller, W. F., Latham, G. V., Nakamura, Y., Toksöz, M. N., Dainty, A. M., et al. (1977). Seismology on Mars. *Journal of Geophysical Research, 82(28),* 4524–4546. https://doi.org/10.1029/JS082i028p04524

Banfield, D., Rodriguez-Manfredi, J. A., Russell, C. T., Rowe, K. M., Leneman, D., Lai, H. R., et al. (2019). InSight Auxiliary Payload Sensor Suite (APSS). Space Science Reviews (Vol. 215). *Springer Nature B.V.* https://doi.org/10.1007/s11214-018-0570-x

Bensen, G. D., Ritzwoller, M. H., Barmin, M. P., Levshin, A. L., Lin, F., Moschetti, M. P., et al. (2007). Processing seismic ambient noise data to obtain reliable broad-band surface wave dispersion measurements. *Geophysical Journal International*, *169*(3), 1239–1260. https://doi.org/10.1111/j.1365-246X.2007.03374.x

Beyreuther, M., R. Barsch, L. Kischer, T. Megies, Y. Behr, & J. Wassermann (2010). ObsPy: A Python toolbox for seismology, *Seismol. Res. Lett*. 81, no. 3, 530–533. https://doi.org/10.1785/gssrl.81.3.530

Foti, S., Lai, G. C., Rix, G. J., & Strobbia, C. (2014). Surface wave methods for near-surface site characterization. London: CRC Press. https://doi.org/10.1201/b17268

Golombek, M., Kipp, D., Warner, N., Daubar, I. J., Fergason, R., Kirk, R. L., et al. (2017). Selection of the InSight Landing Site. *Space Science Reviews*, *211*(1–4), 5–95. https://doi.org/10.1007/s11214-016-0321-9

Harkrider, D. G. (1970). Surface waves in multilayered elastic media. Part II. Higher mode spectra and spectral ratios from point sources in plane layered earth models. *Bull. Seismol. Soc. Am*. 60, 1937–1987.

Hayashi, K. (2008). Development of surface-wave methods and its application to site investigations: Ph.D. dissertation, Kyoto University.

InSight Mars SEIS Data Service. (2019). SEIS raw data, Insight Mission. IPGP, JPL, CNES, ETHZ, ICL, MPS, ISAE-Supaero, LPG, MFSC. https://doi.org/10.18715/SEIS.INSIGHT.XB_2016

Knapmeyer-Endrun, B., Golombek, M. P., & Ohrnberger, M. (2017). Rayleigh Wave Ellipticity Modeling and Inversion for Shallow Structure at the Proposed InSight Landing Site in Elysium Planitia, Mars. *Space Science Reviews*, *211*(1–4), 339–382. https://doi.org/10.1007/s11214-016-0300-1

Larose, E., Khan, A., Nakamura, Y., & Campillo, M. (2005). Lunar subsurface investigated from correlation of seismic noise. *Geophysical Research Letters*, *32*(16), 1–4. https://doi.org/10.1029/2005GL023518

Lepore, S., Markowicz, K., & Grad, M. (2016). Impact of wind on ambient noise recorded by seismic array in northern Poland. *Geophysical Journal International*, *205*(3), 1406–1413. https://doi.org/10.1093/gji/ggw093

Lognonné, P., Banerdt, W. B., Giardini, D., Pike, W. T., Christensen, U., Laudet, P., et al. (2019). SEIS: Insight's Seismic Experiment for Internal Structure of Mars. *Space Science Reviews* (Vol. 215). https://doi.org/10.1007/s11214-018-0574-6

Lognonné, P., Banerdt, W. B., Pike, W. T., Giardini, D., Christensen, U., Garcia, R. F., et al. (2020). Constraints on the shallow elastic and anelastic structure of Mars from InSight seismic data. *Nature Geoscience*, *13*(3), 213–220. https://doi.org/10.1038/s41561-020-0536-y

Longuet-Higgins, M., 1950. A theory of the origin of microseisms, Phil. Trans. R. Soc., 243, 1–35.

Minato, S., Tsuji, T., Ohmi, S., & Matsuoka, T. (2012). Monitoring seismic velocity change caused by the 2011 Tohoku-oki earthquake using ambient noise records. *Geophysical Research Letters*, *39*(9), 1–6. https://doi.org/10.1029/2012GL051405

Murdoch, N., Mimoun, D., Garcia, R. F., Rapin, W., Kawamura, T., Lognonné, P., et al. (2017). Evaluating the Wind-Induced Mechanical Noise on the InSight Seismometers. *Space Science Reviews*, 211, 429-455.

Nakamura, Y. & Anderson, D. L. (1979). Martian wind activity detected by a seismometer at Viking Lander 2 site. *Geophys. Res. Lett., 6*: 499-502. https://doi.org/10.1029/GL006i006p00499

Nakata, N., Gualtieri, L., & Fichtner, A. (2019). Seismic Ambient Noise, Cambridge University Press, Cambridge, UK.

Nimiya, H., Ikeda, T., & Tsuji, T. (2017). Spatial and temporal seismic velocity changes on Kyushu Island during the 2016 Kumamoto earthquake. *Science Advances*, *3*(11). https://doi.org/10.1126/sciadv.1700813

Nishida, K., Kawakatsu, H., & Obara, K. (2008). Three-dimensional crustal S wave velocity structure in Japan using microseismic data recorded by Hi-net tiltmeters. *Journal of Geophysical Research: Solid Earth*, *113*(10), 1–22. https://doi.org/10.1029/2007JB005395

Peterson, J. (1993). Observations and modeling of seismic backgroundnoise,*U.S. Geol. Surv. Open File Report,* 93-322. https://doi.org/10.3133/ofr93322

Roux, P., Sabra, K. G., Kuperman, W. A., & Roux, A. (2005). Ambient noise cross correlation in free space: Theoretical approach. *The Journal of the Acoustical Society of America*, *117*(1), 79–84. https://doi.org/10.1121/1.1830673

Saito, M., 1988. DISPER80: a subroutine package for calculation of seismic normal‐mode solution. in Seismological Algorithm, ed. Doorbos, D.J., Academic Press, San Diego , CA .

Smith, M. D., Wolff, M. J., Spanovich, N., Ghosh, A., Banfield, D., Christensen, P. R., et al. (2006). One Martian year of atmosphericobservations using MER Mini‐TES. *Journal of Geophysical Research*, 111, E12S13. https://doi.org/10.1029/2006JE002770

Spiga, A., Banfield, D., Teanby, N. A., Forget, F., Lucas, A., Kenda, B., et al. (2018). Atmospheric Science with InSight. *Space Science Reviews* (Vol. 214). Springer Nature B.V. https://doi.org/10.1007/s11214-018-0543-0

Takagi, R., Nishida, K., Maeda, T., & Obara, K. (2018). Ambient seismic noise wavefield in Japan characterized by polarization analysis of Hi-net records. *Geophysical Journal International*, *215*(3), 1682–1699. https://doi.org/10.1093/gji/ggy334

Tanimoto, T., Eitzel, M. V., & Yano, T. (2008). The noise cross-correlation approach for Apollo 17 LSPE data: Diurnal change in seismic parameters in shallow lunar crust. *Journal of Geophysical Research E: Planets*, *113*(8), 1–12. https://doi.org/10.1029/2007JE003016

Tokimatsu, K. (1997). Geotechnical site characterization using surface waves. in Earthquake Geotechnical Engineering, K. Ishihara (Editor), A. Balkema, Rotterdam, The Netherlands, 1333–1368.

Wapenaar, K., & Fokkema, J. (2006). Green’s function representations for seismic interferometry. *Geophysics*, *71*(4). https://doi.org/10.1190/1.2213955

Warner, N. H., Golombek, M. P., Sweeney, J., Pivarunas, A. (2016). Regolith thickness estimates from the size frequency distribution of rocky ejecta craters in southwestern Elysium Planitia, Mars, in *47th Lunar and Planetary Science Conference*, Abstract 2231.

Weaver, R. L., & Lobkis, O. I. (2004). Diffuse fields in open systems and the emergence of the Green's function (L). *The Journal of the Acoustical Society of America*, *116*(5), 2731–2734. https://doi.org/10.1121/1.1810232

Witze, A. (2019). "Marsquakes" reveal red planet's hidden geology. *Nature*, *576*(7787), 348. https://doi.org/10.1038/d41586-019-03796-7

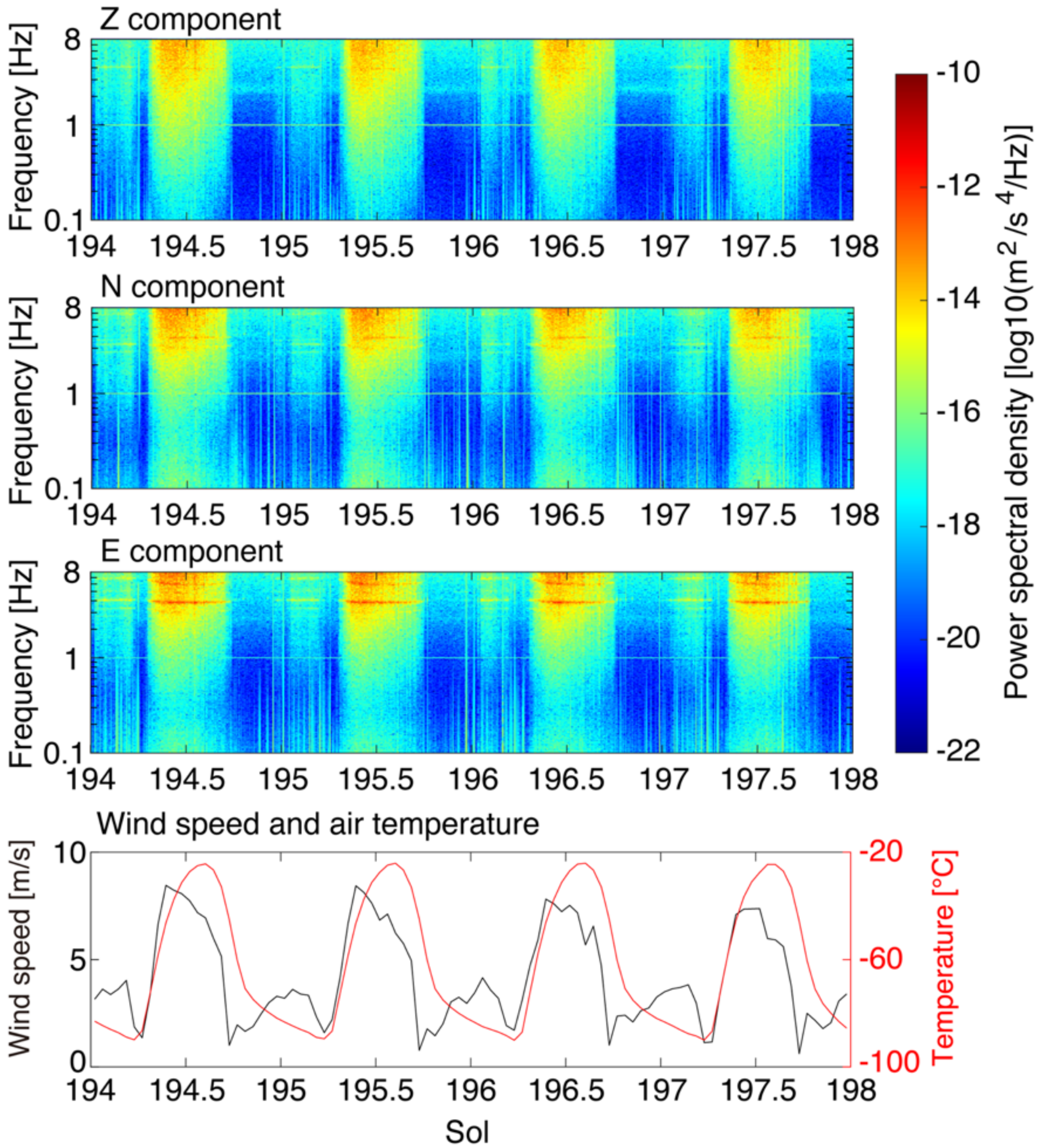

Fig. 1. Temporal variation of power spectral density in the vertical and two horizontal components from Sols 194 to 197. The bottom figure shows the temporal variation of wind speed and air temperature.

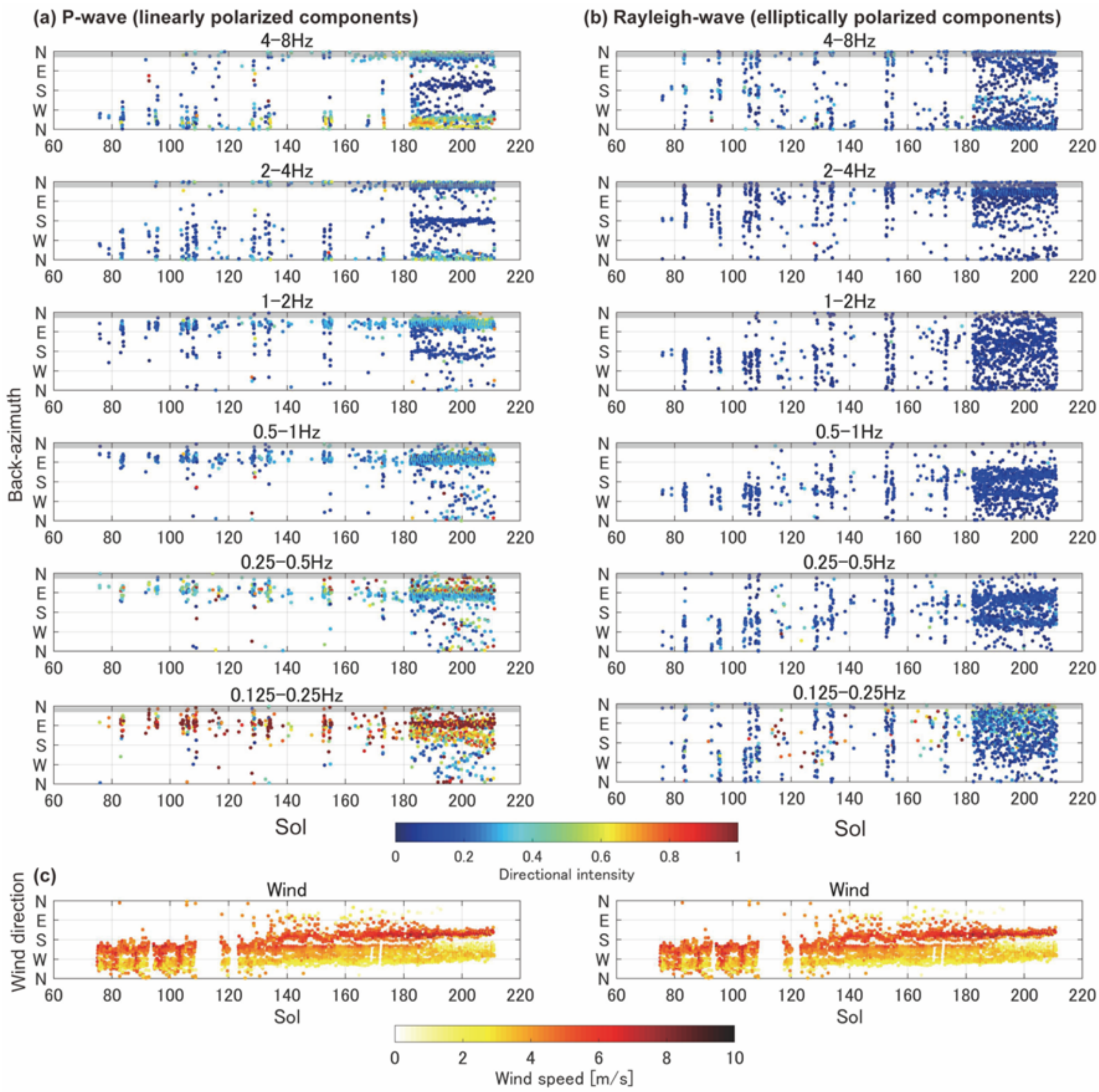

Fig. 2. Temporal variation of dominant back-azimuths and directional intensity of (a) P-waves (linearly polarized components) and (b) Rayleigh waves (elliptically polarized components) in six single-octave frequency bands between Sols 75 and 211. (c) The wind speed and direction during the same period. The gray bar at the top of each back-azimuth plot indicates the direction of the tether connection between the seismometer and the lander (i.e., lander direction; Lognonné et al., 2020).

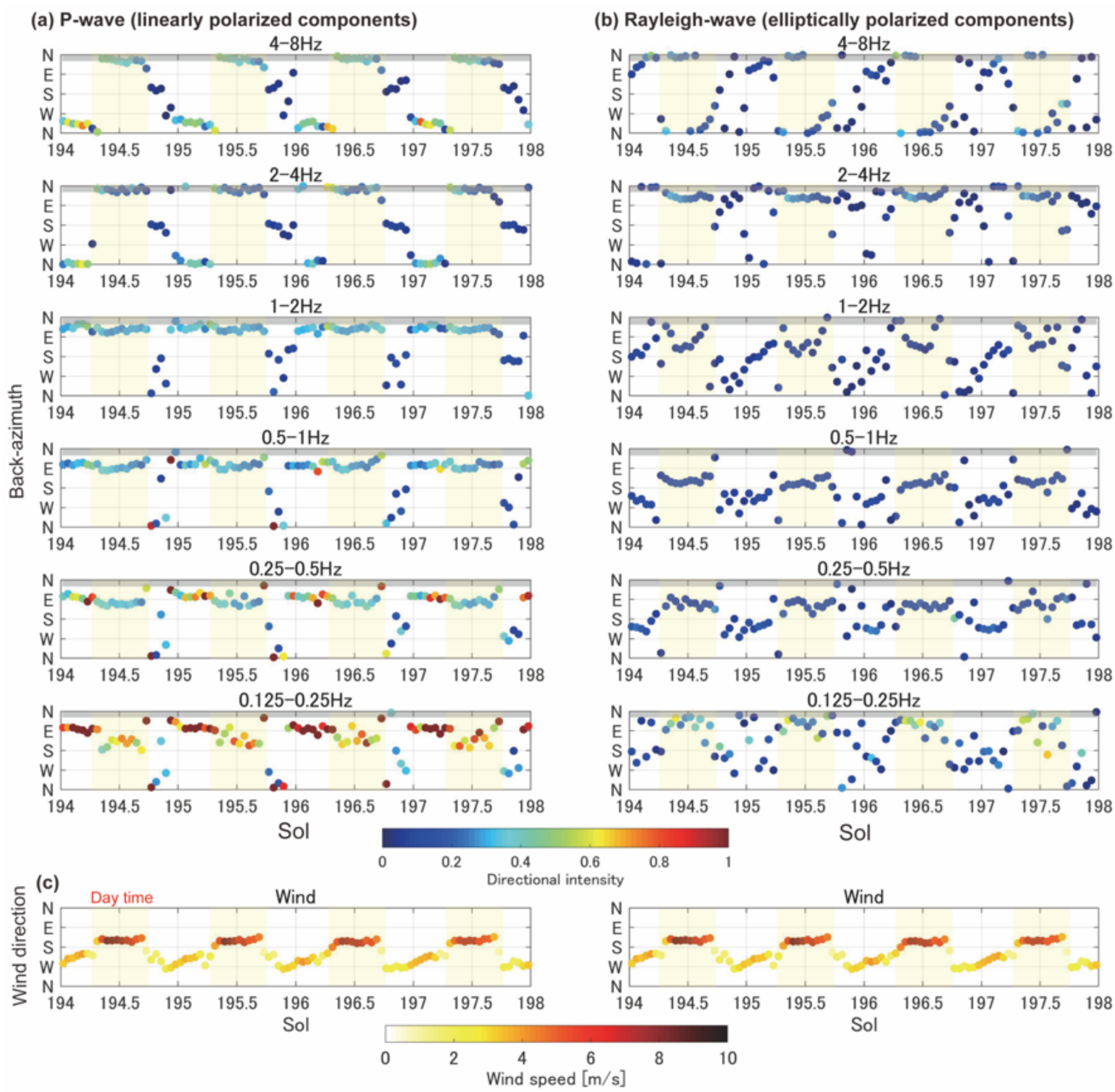

Fig. 3. Temporal variations from Sols 194 to 197 in the dominant back-azimuths and directional intensity of (a) P-waves (linearly polarized components) and (b) Rayleigh waves (elliptically polarized components). (c) The wind speed and direction during the same period. Yellow shaded areas indicate daytime. The gray bar at the top of each back-azimuth plot indicates the direction of the tether connection between the seismometer and the lander (i.e., lander direction; Lognonné et al., 2020).

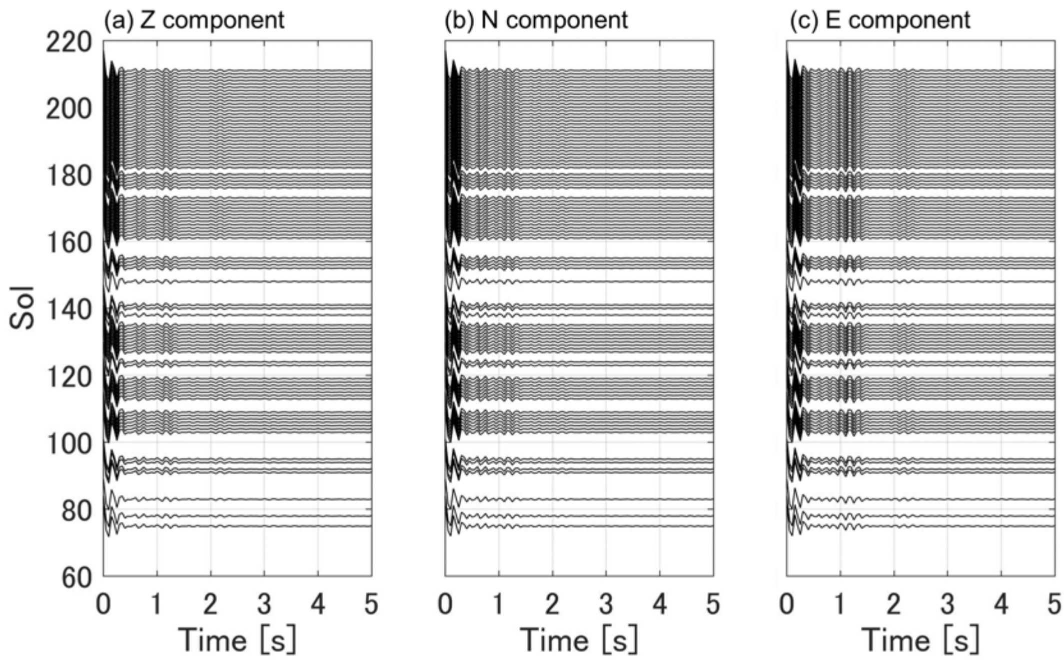

Fig. 4. Temporal variation of autocorrelation functions of components from Sols 75 to 211: (a) Vertical component; (b) NS component; (c) EW component. The vertical component could be similar to P-wave reflectivity whereas the NS and EW components could be S-wave reflectivity.